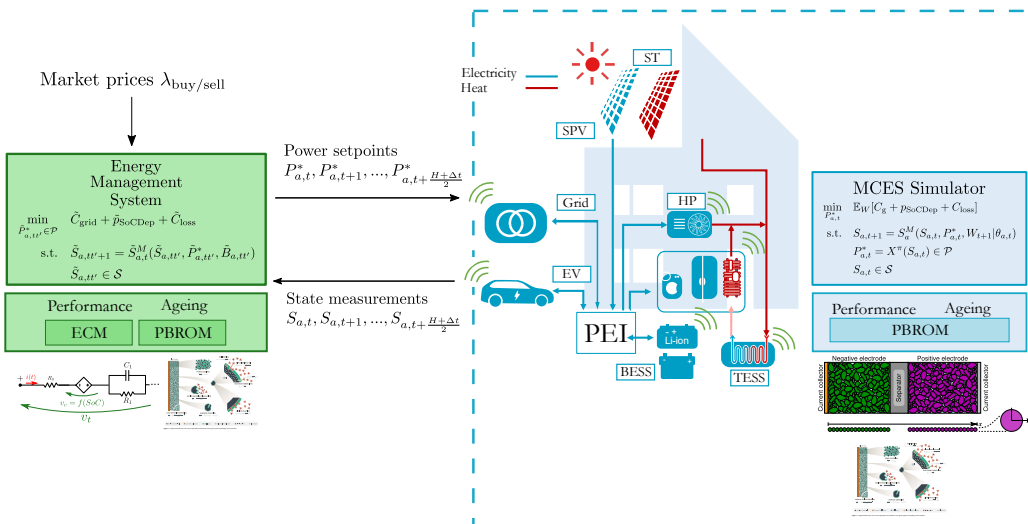


# Graphical Abstract

## Aging-aware Energy Management for Residential Multi-Carrier Energy Systems

Darío Slaifstein, Gautham Ram Chandra Mouli, Laura Ramirez-Elizondo, Pavol Bauer

arXiv:2503.16139v1 [eess.SY] 20 Mar 2025



# Highlights

## **Aging-aware Energy Management for Residential Multi-Carrier Energy Systems**

Darío Slaifstein, Gautham Ram Chandra Mouli, Laura Ramirez-Elizondo, Pavol Bauer

- Contribution on integrating physics-based degradation models into energy management systems for multicarrier buildings.
- Enhanced modeling techniques improve the operation unlocking cost reductions (grid or storage capacity fade).
- Cathode chemistry and aging agnostic energy management algorithm.

# Aging-aware Energy Management for Residential Multi-Carrier Energy Systems

Darío Slaifstein<sup>a</sup>, Gautham Ram Chandra Mouli<sup>a</sup>, Laura Ramirez-Elizondo<sup>a</sup>, Pavol Bauer<sup>a</sup>

<sup>a</sup>*DC Systems, Energy Conversion & Storage, Electrical Sustainable Energy Department, Delft University of Technology, Mekelweg 8, Delft, 2628, Zuid-Holland, Netherlands*

---

## Abstract

In the context of building electrification, the operation of distributed energy resources integrating multiple energy carriers (electricity, heat, mobility) poses a significant challenge. Such an operation calls for an energy management system that decides the set points of the primary control layer in the best way possible. This is has to fulfill user requirements, minimizing costs, and balancing local generation with energy storage. Such storage enables building flexibility. This paper presents a novel aging-aware strategy for electrified buildings. The energy management algorithm presented incorporates physics-based battery aging models to enhance the operational performance, making explicit the trade-off between the grid cost and battery degradation. The proposed algorithm can be used to improve grid costs or to protect the batteries (static or electric vehicle). This energy management algorithm can control different cathode chemistries as well as aged and fresh batteries, improving costs with respect to benchmarks for these cases.

*Keywords:* energy management, battery degradation

*PACS:* 0000, 1111

*2000 MSC:* 0000, 1111

---

## 1. Introduction

The decarbonization of the economy as a whole is a significant challenge for modern societies. In particular, the sustainable transformation of both the energy and transport sectors poses significant technical and cultural challenges [1]. Both transitions meet/couple in the population's homes where electricity, mobility, or heat are needed. Thus, possible synergies (if they exist) between the three systems can be exploited to achieve the desired decarbonization, freedom, resiliency, and cost savings at the local or aggregated level [2]. The successful exploitation of such coupling thus needs to be carefully tailored and built into the design of modern multicarrier energy systems [2–9]. This necessarily leads to advanced energy management systems (EMS) that schedule and control the distributed energy resources (DER) [6, 9–12]. Thus, the EMS needs to handle uncertain and variable forecasts (electric vehicles [13], solar), aging assets (batteries [14–18]), and user preferences.

To dispatch and operate such systems, the literature suggests Model Predictive Control (MPC) [6, 12], stochastic optimization [19], reinforcement learning (RL) [6, 7, 9] and many others. Nevertheless, the basis of such advanced systems is usually a day-ahead plan or dispatch that schedules the power of the assets along the day [4, 10, 11, 20]. This planner is usually an optimization-based system that uses approximated deterministic forecasts of certain inputs to schedule the different assets. The decisions taken are then implemented (and modified if necessary) in real time. For a residential multicarrier energy systems (MCES) such as the one presented in Fig. 1, the assets can generate, consume, or store energy from/in different carriers (electricity, heat, and transport). Controllable assets (loads or generation) combined with energy storage systems (ESS) en-

able flexibility from the building, and thus, their operation and modeling are crucial in reducing safety margins and unlocking additional cost savings.

To coordinate hybrid energy storage system (HESS), the different technologies must be modeled accordingly, properly representing their different power limits, dynamics, and particularities. In particular battery ESS technologies are limited by their aging [5, 10, 15–18, 21], (Li-ion batteries (LIB) and electric vehicle (EV)), as well as by their availability for mobility (EV) [5, 13]. Unfortunately, although aging mechanisms have been studied and modeled [5, 14, 22–25], they have not been entirely incorporated into EMS design of residential MCES [5, 10].

Energy management system formulations of residential MCES tend to simplify the models used to linear or quadratic models, overlooking most technology particularities [2, 6, 9, 26]. White-box models are usually reserved for HVAC systems, focusing on thermal comfort [20, 26], and not to the ESS. Ceusters et al. [6, 7] only use first-order linear models for both battery energy storage system (BESS) and thermal energy storage system (TESS), neglecting any differences between their dynamics. Similarly, Ye et al. [9] does not mention any difference between storage systems nor include EVs in their system. Other works, only focus on the electrical carrier [4, 10, 16] using different types of battery models, used to describe the key variables such as state-of-charge  $SoC$ , terminal voltage  $v_t$ , state-of-health  $SoH$ . However, a possible link to the thermal carrier is not explored.

Aging models fall within two categories: empirical or physics-based (PB) [5, 17]. The first are the most widely used in the literature due to their simplicity. They are obtained by performing long standardized calendar and cycling ageing tests

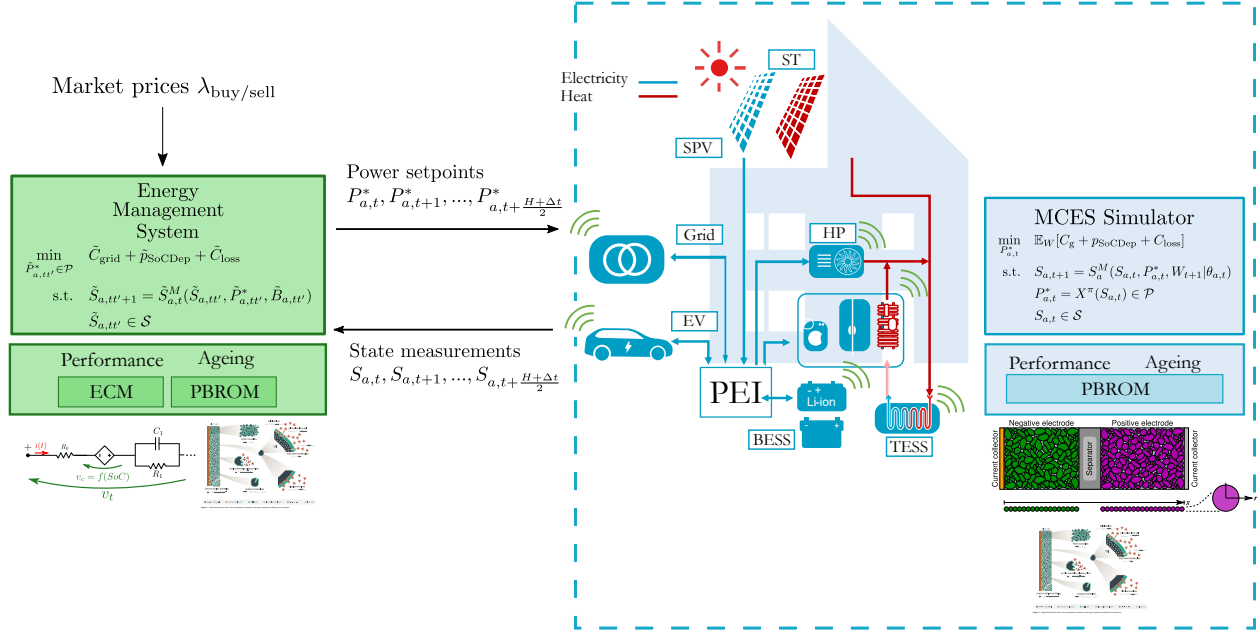


Figure 1: Schematic diagram of the proposed electrified multi-carrier building.

[5, 21]. Unfortunately, empirical degradation models only have interpolation capabilities, usually use non-linear equations, represent a limited number of operating conditions (average C-rate, minimum  $SoC$ , etc.), are prone to overfitting and are chemistry dependent [5, 25]. On the other hand, PB models are built through first-principles and specialized tests to identify individual degradation mechanisms [21, 22]. They have extrapolation features, can be expressed in the state-space form (or similar), account for several cathode chemistries and represent a wide range of operating conditions. However, they are also non-linear and, in general, non-convex [21–24, 27]. The integration of PB aging models into the operation of BESS has been recently studied at the battery management system (BMS) level for standalone and EV applications [14–16, 28, 29] usually through control-oriented physics-based reduced order model (PBROM). To the author’s best knowledge, their integration into wider schemes, such as transmission grids, microgrids, buildings, or industry, has not been extensively researched yet.

The contribution of this paper is the integration of PBROM aging models into EMS day-ahead planning algorithms in the context of residential MCES. PBROM aging models give the EMS enough information to:

- handle different cathode chemistries.
- seamlessly operate new and used batteries
- identify dominant degradation mechanisms.

Our planning algorithm is an optimization-based secondary controller that minimizes energy cost and battery aging. A schematic of the MCES is presented in Fig. 1. The system is composed of solar photovoltaics (SPV), BESS, EV, power electronic interface (PEI), heat pump (HP), solar thermal (ST), TESS, grid connection and loads.

This paper is organized as follows: section 2 presents the problem and modelling framework, section 3 presents the algorithm design and models used; section 4 explains the simulator; section 5 describes our case studies and validation; finally section 6 presents the conclusions and shortcomings of this approach.

## 2. Modeling and Optimal Planner

The following section describes the EMS models, following the Universal Modeling Framework (UMF) by Powell [30–32]. For a given system size the objective is to handle the operation cost, which is composed of three parts: the net cost of energy from the grid  $C_{grid}$ , the degradation cost of losing storage capacity  $C_{loss}$ , and a penalty for not charging the EV  $p_{SoCDep}$ . The grid cost and the degradation cost are cumulative objectives because the goal is to optimize them through time, while the penalty for not charging the EV to the desired  $SoC$  is only a point reward at departure times  $t_{dep}$ . The sequential decision problem (SPD) is then:

$$\begin{aligned} \min_{P_{a,t}^*} \quad & \mathbb{E}_W[C_{grid} + C_{loss} + p_{SoCDep}] \\ \text{s.t.} \quad & S_{a,t+1} = S_a^M(S_{a,t}, P_{a,t}^*, W_{t+1}|\theta_{a,t}) \\ & P_{a,t}^* = X_t^\pi(S_{a,t}) \in \mathcal{P} \quad \forall a \in \mathbb{A} \\ & S_{a,t} \in \mathcal{S} \quad \forall a \in \mathbb{A} \end{aligned} \quad (1)$$

with

$$\mathbb{A} = \{\text{SPV, grid, EV, BESS, HP, ST, TESS}\}. \quad (2)$$

where the components of the objective are:

$$C_{grid} = w_{grid} \sum_{t=0}^T (\lambda_{buy,t} \cdot P_{g,t}^+ - \lambda_{sell,t} \cdot P_{g,t}^-) \cdot \Delta t \quad (3)$$

$$C_{\text{loss}} = w_{\text{loss}} \cdot c_{\text{loss}} \cdot \sum_{t=0}^T \sum_{sa} N_{s,sa} \cdot N_{p,sa} \cdot i_{\text{loss},as,t} \cdot \Delta t, \quad \forall sa \subset a, \quad (4)$$

$$P_{\text{SoCDep}} = w_{\text{SoC}} \cdot \|\varepsilon_{\text{SoC},t_{\text{dep}}}\|_2^2 \quad (5)$$

where  $S_{a,t}$  is the state vector,  $P_{a,t}^*$  is the optimal decision for timestep  $t$ ,  $W_{t+1}$  is an exogenous process that introduces new information after making a decision. The mappings  $S_{a,t}^M(\cdot)$ , and  $X_t^\pi(\cdot)$  are the transition function and optimal policy, respectively. The first is a set of equations describing the states and parameter evolution, and the second is the algorithm that finds the setpoints. The vector  $\theta_{a,t}$  contains all the parameters of each asset  $a$  and changes over time  $t$ . The subindex  $a \in \mathbb{A}$  corresponds to the assets shown in Fig. 1. The index  $sa \in \{\text{BESS}, \text{EV}\} \subset a$  denotes the electric storage assets. The time window is  $H$  and the timestep  $\Delta t = 15\text{min}$ .  $C_{\text{loss}}$  is explained in Section 3.1.2 and the penalty  $p_{\text{SoCDep}}$  in Section 3.2.

The following definitions of the elements are considered:

- The state vector has 3 components, the physical state of the system  $R_t$ , other (deterministic) information  $I_t$ , and beliefs about uncertain quantities or parameters  $B_t$ . All the observable physical quantities of our system, such as currents, voltages, and so on are included in  $R_t$ . Other non-physical information, like prices are included in  $I_t$ . Finally, our belief state  $B_{a,t}$  is composed of forecast medians. These are defined as:

$$S_{a,t} = [R_a, I_a, B_a]_t^T, \quad (6)$$

$$B_{a,t} = [\tilde{P}_{\text{PV}}, \tilde{P}_{\text{ST}}, \gamma_{\text{NEV}}, \tilde{P}_{\text{load}}^e, \tilde{P}_{\text{load}}^{\text{th}}]_t^T. \quad (7)$$

- The actions or decision variables are

$$P_{a,t}^* = [P_{\text{EV}}, P_{\text{BESS}}, P_{\text{HP}}^e]_t^T.$$

- The superscripts e and th refer to electricity or thermal carriers. They are used when the subscript is the same.
- Both the actions and state vectors have upper and lower limits denoted as  $\bar{P}_{a,t}^*$ ,  $\underline{P}_{a,t}^*$ ,  $\bar{S}_{a,t}$ , and  $\underline{S}_{a,t}$ .
- All bidirectional powers, either actions or states, are modeled with their converter efficiency  $\eta_a$ :

$$\eta_a S_{a,t}^+ - \frac{1}{\eta_a} S_{a,t}^- = S_{a,t}, \quad (8)$$

with  $S_t^- \perp S_t^+$

- The order of the subscript is "name, device, time index".
- Capital  $C$  denotes total cost in €, lowercase  $c$  denotes unit cost and  $w$  indicates tuning/scaling weight.

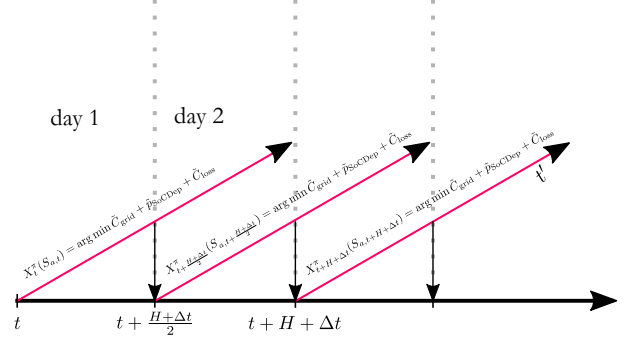


Figure 2: Deterministic DLA policy as a day-ahead planner.

The operation's inputs are the prices  $\lambda_{\text{buy/sell},t}$ , EV availability  $\gamma_{\text{NEV},t}$ , the solar power  $P_{\text{PV},t}$ , the electric demand  $P_{\text{load},t}^e$ , and the thermal demand  $P_{\text{load},t}^{\text{th}}$ . All of them can be considered to be exogenous processes that are known after making a decision.

In Eq. 1 the planner or policy  $\pi$  wants to minimize the likelihood of the operational cost  $\mathbb{E}[C]$  under the exogenous information process  $W$ . The problem at hand is a state-dependent problem in which our decisions  $P_{a,t}^*$  are based on the current  $S_{a,t}$ , and influence future states  $S_{a,t+1}$  (and thus, future decisions). Given the focus on future states and decisions, lookahead policies appear as attractive candidates for solving this SPD. Policy design and models are presented in the following Section 3.

### 3. Policy design

As mentioned before, the SPD in Eq. 1 is a state-dependent problem where current states influence future decisions. As such Direct Lookahead (DLA) policies are commonly used in the literature to solve these problems. Two common examples of this policy family are optimal control strategies and stochastic dual dynamic programming. For this work, we focus on day-ahead planning, which is a subset of optimal control where deterministic inputs (forecast medians in this case) are used to decide the actions for the incoming day. The process is shown in Fig. 2.

More specifically a DLA policy based on the devices' approximated dynamic models. In this way, the EMS plans future actions based on approximate predictive models of devices. Approximation is then denoted with  $\tilde{\cdot}$ . The policy is then solving an approximated economic optimal control problem (OCP) of the form:

$$\begin{aligned} \min_{\tilde{P}_{a,t'}^* \in \mathcal{P}} \quad & \tilde{C}_{\text{grid}} + \tilde{C}_{\text{loss}} + \tilde{p}_{\text{SoCDep}} + \tilde{P}_{\text{TESS}} \\ \text{s.t.} \quad & \tilde{S}_{a,t,t'+1} = \tilde{S}_a^M(\tilde{R}_{a,tt'}, \tilde{I}_{a,tt'}, \tilde{P}_{a,tt'}^*, \tilde{B}_{a,tt'}) \\ & \tilde{S}_{a,t} \in \mathcal{S} \quad \forall a \in \mathbb{A} \end{aligned} \quad (9)$$

where

$$\tilde{P}_{\text{TESS}} = w_{\text{TESS}} \cdot \max(0, S \tilde{\delta} C_{\text{TESS}} - \overline{S \delta C}_{\text{TESS}}) \quad (10)$$

In our policy the upper limit constraint of the TESS,  $S_{oC_{TESS}}$ , is implemented as a soft constraint to avoid infeasibilities during initialization or feedback. The penalty in the objective steers the  $S_{oC_{TESS,t}}$  towards the feasible region when the weight  $w_{TESS}$  is high enough.

The deterministic optimization problem in Eq. 9 approximates the real stochastic one by using forecasts, stored in  $B_{a,t}$ , and approximated models for the transition function  $\tilde{S}_{a,t}^M$ . In this model, the time  $t$  is the time at which the DLA policy is created and  $t'$  is the time inside the policy itself. Note the subtle difference between the approximated dynamics  $\tilde{S}_{a,t}^M$  and the real ones  $S_{a,t}^M$ . This is not to be overlooked because the assumption that the predictions done by the policy  $\pi$  hold true can lead to disappointing results in real-world applications. Making these distinctions early in design reveals important insights for future stages. In this work, the energy management algorithm (EMA) has an approximated model  $\tilde{S}_{a,t}^M$  to decide the setpoints  $\tilde{P}_{a,t'}^*$  to be implemented in a simulator  $S_{a,t}^M$  containing detailed fidelity models. In the future, the simulator might as well grow enough to be considered a digital twin of the real building.

Thus the policy is:

$$X_t^\pi(S_{a,t}) = \arg \min_{P_{a,t}, \dots, P_{a,t+H}} \tilde{C}_{grid} + \tilde{C}_{loss} + \tilde{P}_{SoCDep} + \tilde{P}_{TESS} \quad (11)$$

subject to the approximate transition function  $\tilde{S}_{a,t}^M$ . This encompasses model approximation and forecasting ( $\tilde{B}_{a,t'}$ ) of the future inputs ( $W_{t+1}$ ). The policy is then tuned by changing the weights  $w$  and implementing different NLP solver options (warm-starting, multi-start, etc.)

Notationally, we define a sequence matrix containing power setpoints and states from  $t$  to  $t + H$  with:

$$\mathcal{P}_{a,[t,t+H]} = [P_{a,t}, P_{a,t+1}, \dots, P_{a,t+H}] \quad (12)$$

$$\mathcal{S}_{a,[t,t+H]} = [S_{a,t}, S_{a,t+1}, \dots, S_{a,t+H}] \quad (13)$$

The approximate transition function  $\tilde{S}_{a,t}^M(\cdot)$  is the compendium of the equations specified in the rest of this section.

The thermal assets are modelled in a linear way:

$$P_{HP}^{th} = \eta_{HP} \cdot P_{HP}^e, \quad (14)$$

$$\tilde{P}_{ST} = \eta_{ST} \cdot \tilde{P}_{PV}, \quad (15)$$

and

$$S_{oC_{TESS,t+1}} = S_{oC_{TESS,t}} - \frac{\Delta t}{Q_{TESS} \cdot 3600} \cdot \eta_{TESS} \cdot P_{TESS,t}, \quad (16)$$

where  $\eta$  denotes a conversion factor or efficiency,  $Q_{TESS}$  is the capacity in kWh. The thermal balance comes in as:

$$\tilde{P}_{ST} + P_{HP}^{th} + P_{TESS} = \tilde{P}_{load}^{th}. \quad (17)$$

The electric power balance, on the other hand, is

$$\tilde{P}_{PV} + P_{BESS} + \gamma_{EV} \cdot P_{EV} + P_{grid} = \tilde{P}_{load}^e + P_{HP}^e. \quad (18)$$

where  $\gamma_{EV}$  is the EV availability, explained in Section 3.2.

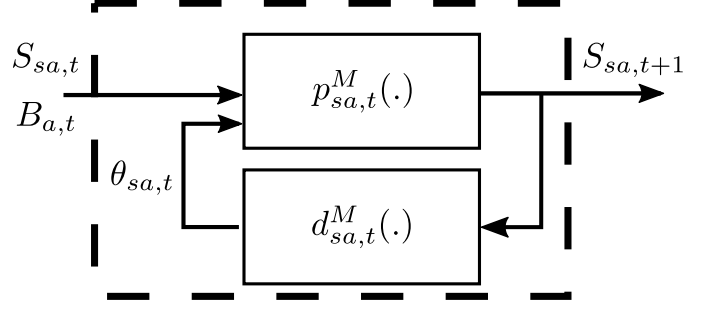


Figure 3: Storage asset transition function diagram  $\tilde{S}_{sa,t}^M$

### 3.1. Batteries

The remaining devices in the MCES are all battery-based ESS. Batteries have complex nonlinear dynamics, and several modeling techniques are presented in the literature [17]. In this work, models coming from empirical and physics-based approaches are used. The modeling is divided into two different sub-models: performance and aging. Under the UMF, this is represented in the transition function  $\tilde{S}_{sa,t}^M(\tilde{S}_{sa,t}, x_{sa,t}|\theta_t)$ , which contains both the perf. model  $p_{sa,t}^M(\cdot)$  and the aging model  $d_{sa,t}^M(\cdot)$ . The performance model predicts stored energy  $S_{oC_{sa,t}}$  and terminal voltage  $v_{t,sa,t}$ . The aging model is used to update the parameters of  $p_{sa,t}^M(\cdot)$ , as shown in Fig. 3.

The perf. model is then:

$$S_{sa,t+1} = p_{sa,t}^M(S_{sa,t}, P_{sa,t}, B_{a,t}|\theta_{sa,t}) \quad (19)$$

where the components of the state depend on the functional form used for the model. In general, this is a nonlinear state space system.

The aging model  $d_{sa,t}^M(\cdot)$  is a set of equations that describe the dynamics of the performance parameters  $\theta_{sa,t}$ .

$$\theta_{sa,t+1} = d_{sa,t}^M(S_{sa,t}, P_{sa,t}, B_{a,t}, \theta_{sa,t}) \quad (20)$$

Finally, a terminal constraint is implemented to ease up feasibility and mitigate symmetries in the OCP of Eq. 9, as in:

$$S_{oC_{BESS,t_1}} = S_{oC_{BESS,t_1+T}} \quad (21)$$

where  $t_0 \leq t_1 \leq T \leq H$ . This way the OCP is better conditioned but the planner still has the freedom to decide  $S_{oC_{BESS,T}}$  [33].

#### 3.1.1. Performance models $p_{sa,t}^M$

For the performance submodel, two alternatives have been implemented: a simple bucket model (BM) and a first order equivalent circuit model (ECM). A basic BM of the operation of a battery assumes that its output voltage  $v_t$  is linear with the state of charge  $S_{oC}$ , assuming no voltage drop. Hence the only equations of this model are

$$S_{oC_{sa,t+1}} = S_{oC_{sa,t}} - \frac{\Delta t}{Q_{sa,t} \cdot 3600} \cdot \eta_c \cdot i_{sa,t}, \quad (22)$$

$$i_{sa,t} = \frac{P_{sa,t}}{v_{t,sa,t} \cdot N_{s,sa} \cdot N_{p,sa}}, \quad (23)$$

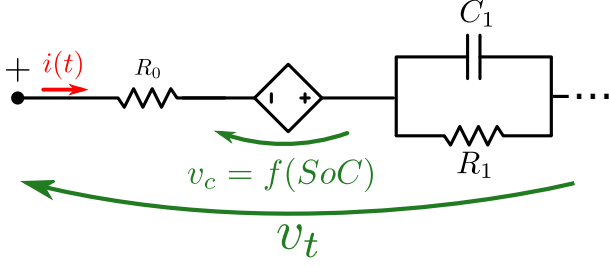


Figure 4: First order Equivalent Circuit Model.

$$OCV_{sa,t} = a_{OCV,sa} + b_{OCV,sa} \cdot SoC_{sa,t}, \quad (24)$$

$$v_{t,sa,t} = OCV_{sa,t}, \quad (25)$$

$$S_{sa,t} = [SoC_{sa}, v_{t,sa}, i_{sa,t}]^T \quad (26)$$

where  $i_{sa,t}$  is the current passing through the cell,  $OCV_{sa,t}$  is the open circuit voltage,  $\eta_c$  is the Coulombic efficiency [18] and  $Q_{sa,t}$  is the cell capacity in Ah. Each battery pack is assumed to be organized as a series connected module (SCM) where  $N_{s/p, sa}$  are the series cells per branch and parallel branches, respectively. In this model, the most relevant parameter in  $\theta_{sa}$  is the  $Q_{sa}$ .

A first-order ECM has improved accuracy due to the incorporation of diffusion and series resistance, Fig. 4. The performance sub-model  $p_{sa,t}^M(\cdot)$  is then modified by adding the equation:

$$i_{R1,sa,t+1} = e^{-\frac{\Delta t}{R1,sa \cdot C1,sa}} \cdot i_{R1,sa,t} + \left(1 - e^{-\frac{\Delta t}{R1,sa \cdot C1,sa}}\right) \cdot i_{sa,t} \quad (27)$$

and modifying Eq. 25 as in:

$$v_{t,sa,t} = OCV_{sa,t} - i_{R1,sa,t} \cdot R1,sa - i_{sa,t} \cdot R0,sa, \quad (28)$$

where  $i_{R1,sa,t}$  is the pole current. Eqs. 22, 23 and 24 are maintained. The ECM incorporates the series voltage drop that limits power output and the first-order diffusion dynamics. Here the relevant parameters are  $\theta = [Q, R0]^T$  which usually define the cell's state of health  $SoH$ .

### 3.1.2. Degradation models $d_{sa,t}^M(\cdot)$

For the aging models, the first alternative is an empirical sub-model presented by [25]. The empirical sub-model reduces all the degradation mechanisms into calendar and cyclic aging.

$$i_{cycle,sa,t} = \frac{c1 \cdot c3}{c4} \cdot e^{c2 \cdot |i_{sa,t}|} \cdot (1 - SoC_{sa,t}) \cdot |i_{sa,t}|, \quad (29a)$$

$$i_{cal,sa,t} = c5 \cdot e^{-\frac{24 \cdot kJ}{RT}} \cdot \sqrt{t}, \quad (29b)$$

$$i_{loss,sa,t} = i_{cycle,sa,t} + i_{cal,sa,t}, \quad (29c)$$

and

$$Q_{sa,t+1} = Q_{sa,t} - \frac{\Delta t}{3600} \cdot i_{loss,sa,t}. \quad (30)$$

For the physics-based alternative, the reduced order model (PBROM) from [15] is used. It accounts for two degradation mechanisms: the solid electrolyte interface (SEI) and active

material loss (AM). The author also presents a PBROM for Li-plating but its particular functional form prevents it from being implemented inside a MINLP solved by an interior-point solver.

The growth of the SEI layer is modeled with a general reaction that aims to average all the different byproducts that compose the SEI layer. This is synthesized in the reversible SEI current  $i_{SEI}$ :

$$i_{SEI,sa,t} = \frac{k_{SEI,sa} \cdot e^{-\frac{E_{SEI,sa}}{RT}}}{n_{SEI} \cdot (1 + \lambda_{sa} \cdot \beta_{sa}) \cdot \sqrt{t}} \quad (31)$$

where  $k_{SEI}$  is the kinetic rate of the average reaction,  $E_{SEI}$  is the activation energy of the reaction,  $n_{SEI}$  is the average number of  $e^-$  transferred with the layer and  $\lambda$  and  $\beta$  are parameters depending on other variables such as  $\eta_k$ ,  $OCV_n$ ,  $z$  and others.

The system is completed with:

$$\eta_{k,sa,t} = \frac{2 \cdot R \cdot T}{F} \cdot \sinh^{-1} \left( \frac{i_{sa,t}}{n_{SEI} \cdot a_s \cdot A \cdot L_n \cdot i_0} \right) \quad (32)$$

$$z_{sa,t} = SoC_{sa,t} \cdot (z_{100\%} - z_{0\%}) + z_{0\%} \quad (33)$$

$$\beta_{sa} = e^{\frac{n_{SEI} \cdot F}{R \cdot T} \cdot (\eta_{k,sa} + OCV_{n,sa} - OCV_s)} \quad (34)$$

where  $\eta_k$  is the SEI side reaction kinetic overpotential,  $z$  is the Li stoichiometry of the cell,  $OCV_n$  is the open-circuit voltage of the anode made with an empirical fit,  $OCV_s = 0.4V$  is the side reaction open-circuit voltage, and  $T$  is the cell temperature. It is assumed that the temperature  $T$  is constant over time and is controlled by the local primary control system. The rest of the parameters can be found in the Appendix A.

The loss of active material due to the mechanical stress of the electrode is modeled with:

$$i_{AM,sa,t} = k_{AM,sa} \cdot e^{-\frac{E_{AM,sa}}{RT}} \cdot SoC_{sa,t} \cdot |i_{sa,t}| \cdot Q_{sa}, 0 \quad (35)$$

The total aging is the contribution of both mechanisms SEI layer growth and AM loss. The capacity fade current is:

$$i_{loss,sa,t} = i_{SEI,sa,t} + i_{AM,sa,t} \quad (36)$$

which is later used again in 30.

Now, by carefully inspecting Eq. 28, the reader will notice that if  $R0,sa,t$  is incorporated as a variable in the OCP, Eq. 9, this would add another non-convex constraint to it (since  $i_{sa,t}$  can be either positive or negative). Thus, its evolution is only included in the simulator  $S_{a,t}^M(\cdot)$  updating the parameters without the policy  $X_t^T$  being directly aware of the process.

To model the power fade (i.e. the increase of  $R0$ ), the SEI layer thickness  $\delta_{SEI, sa, t}$  growth is described by:

$$\delta_{SEI,sa,t+1} = \delta_{SEI,sa,t} + \frac{\Delta t}{M_{SEI} \cdot n_{SEI} \cdot F \cdot \rho_{SEI} \cdot A_n} \cdot i_{SEI,sa,t} \quad (37)$$

Hence the dynamics of the series resistance  $R0$  are:

$$R0,sa,t+1 = R0,sa,t + \frac{\epsilon_s}{k_{eff}} \cdot \frac{\Delta t}{M_{SEI} \cdot n_{SEI} \cdot F \cdot \rho_{SEI} \cdot A_n} \cdot i_{SEI,sa,t} \quad (38)$$

The solvent S leaves the electrolyte to form the SEI layer thus, the volume fraction of S evolves with:

$$\epsilon_{e,sa,t+1} = \epsilon_{e,sa,t} - a_s \cdot \frac{\Delta t}{M_{SEI} \cdot n_{SEI} \cdot F \cdot \rho_{SEI} \cdot A_n} \cdot i_{SEI,sa,t} \quad (39)$$



---

**Algorithm 1** MCES simulation
 

---

- 1: **Define setpoint sequences**  $\mathcal{P}_{a,[t,t+(H+\Delta t)/2]}$
  - 2: **Define exogenous information sequences**  $\mathcal{W}_{[t+1,t+1+(H+\Delta t)/2]}$
  - 3: Recalculate  $P_{\text{TESS},t}$  and  $P_{\text{grid},t}$  with Eqs. 17, 18,  $\mathcal{P}_{a,[t,t+(H+\Delta t)/2]}$ , and  $\mathcal{W}_{a,[t+1,t+1+(H+\Delta t)/2]}$
  - 4: **for**  $t \in \mathcal{D}_t$  **do**
  - 5:   Simulate  $S o C_{\text{TESS},t}$  using Eq. 16
  - 6:   Simulate  $sa$  performance using  $p_{sa}^M(\cdot)$  PBROM [35]
  - 7:   Simulate  $sa$  degradation using  $d_{sa,t}^M(\cdot)$  PBROM [15]
  - 8: **end for**
  - 9: Feed-back  $\mathcal{S}_{a,[t,t+(H+\Delta t)/2]}$  to the planner
- 

### 3.2. Electric Vehicle

From the point of view of a residential building, the EVs are a BESS with availability constraints and certain requirements regarding their  $S o C$  at departure time  $t_{\text{dep}}$ . For the availability  $\gamma$ , the probability distributions of departure ( $t_{\text{dep}}$ ) and arrival ( $t_{\text{arr}}$ ) times can be described as random variables  $t_{\text{dep/arr}} \sim \mathcal{T}_{\text{dep/arr}}$ , whose distributions  $\mathcal{T}_{\text{dep/arr}}$  are taken from Elaad [34]. The availability  $\gamma_t$  will then be:

$$\gamma_t = \begin{cases} 0 & t \in [t_{\text{dep}}; t_{\text{arr}}] \\ 1 & \text{otherwise} \end{cases}. \quad (40)$$

The power balance of an EV is

$$P_{\text{tot,EV},t} = \gamma_{\text{EV},t} P_{\text{EV},t} + (1 - \gamma_{\text{EV},t}) P_{\text{drive,EV}} \quad (41)$$

where  $P_{\text{tot,EV},t}$  is the total power of the EV,  $P_{\text{EV},t}$  is the charger power, and  $P_{\text{drive,EV}}$  is the power consumed driving assuming no public charging. The total power  $P_{\text{tot,EV},t}$  is then used in Eq. (23) and later for calculating the aging of the EV batteries. The average driving power is also sampled from a Gaussian distribution  $P_{\text{drive,EV}} \sim \mathcal{N}(\mu_{\text{drive}}, \sigma_{\text{drive}}^2)$ . This is because the EV battery pack degradation during driving needs to be accounted for in the operation strategy (charging and driving)

At  $t_{\text{dep}}$  the EV is required to be delivered at  $S o C_{\text{dep}}^*$ :

$$S o C_{\text{EV}}(t_{\text{dep}}) = S o C_{\text{dep}}^* \quad (42)$$

This is implemented as a penalty in the objective function, Eq. 9, as in any typical OCP. The deviation from the reference at the desired time is penalized with:

$$\varepsilon_{S o C} = S o C_{\text{EV}}(t_{\text{dep}}) - S o C_{\text{dep}}^* \quad (43)$$

where  $w_{S o C}$  is a weight chosen by the user.

### 4. MCES Simulator $S_{a,t}^M(\cdot)$

The simulator is used to evaluate the policy  $\pi$  and close the loop with the state measurements. It is designed to:

- Provide high-accuracy simulation results that act as plant measurements.

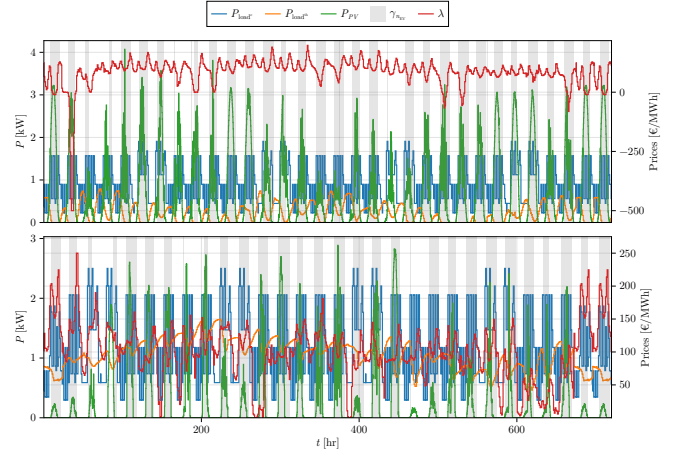


Figure 5: Exogenous information  $W_{t+1}$ . Grey bands represent periods where the EV is not connected.

- Adjust/reject setpoints that violate hard constraints.
- Re-balance power in case of rejections or infeasible optimizations.

The whole process is defined in Algorithm 1. First, the power setpoints must be adjusted for the grid and TESS because the forecast used in  $X_t^r$  will never be the same as the actual exogenous inputs. Take a look at the balances, Eq. 17 and 18, which contain the loads and solar generation. It is clear that  $\tilde{P} \neq P$  and a device must compensate for that difference. Thus, the simulator  $S_{a,t}^M$  recalculates:

$$P_{\text{TESS},t} = P_{\text{load},t}^{\text{th}} - P_{\text{ST},t} - P_{\text{HP},t}^{\text{th}}. \quad (44)$$

$$P_{\text{grid},t} = P_{\text{load},t}^{\text{c}} + P_{\text{HP},t}^{\text{c}} - P_{\text{PV},t} - P_{\text{BESS},t} - \gamma_{\text{EV},t} P_{\text{EV},t}. \quad (45)$$

Second, once these powers have been adjusted, the simulator uses them to obtain the true/actual/fidelity state sequence  $\mathcal{S}_{a,[t,t+(H+\Delta t)/2]}$ . For the TESS it recalculates Eq. 16. For the  $sa$ , it uses LiIBRA.jl [35] to swiftly simulate PBROMs of the performance of the battery [17, 36]. After that, the models from Jin [15] are used to calculate the true degradation outcome of the decisions  $P_{a,t}^*$ . Again, the reader must remember that the capacity fade (decrease in  $Q_{sa,t}$ ) is modeled in both the simulator  $S_{a,t}^M$  and the approximate model of the planner  $\tilde{S}_{a,t}^M$ , whereas the power fade (increase in  $R_{0,as,t}$ ) is only addressed in the simulator  $S_{a,t}^M$ . Finally, if an action  $P_{sa,t}^*$  causes a future state to go out of bounds ( $S_{sa,t+1} \leq \underline{S}_{sa}$  or  $S_{sa,t+1} \geq \overline{S}_{sa}$ ), the action is rejected and the  $sa$  remains in that state (either  $\overline{S}_{sa}$  or  $\underline{S}_{sa}$ ) until the next day. Finally, the carriers are re-balanced if necessary.

The final state sequence is then fed back to the optimization-based planner. For practical implementation, in which the simulator is, in fact, an experimental setup, an online state observer is necessary to feed back the states to the EMS. This is particularly important for the ESS [17, 18, 37].

### 5. Case studies

The building has a grid connection with a smart meter with 15min resolution. The connection is also the physical link to



---

**Algorithm 2** Rolling horizon algorithm

---

- 1: **Initialize hyperparameters**  $t_0, \Delta t, t_W, w, d$
  - 2: **Initialize device states and inputs**  $S_{a,0}$
  - 3: **for**  $d \in 1 : n_d$  **do**
  - 4:   Solve the deterministic OCP, Eq. 9, and obtain  $P_{a,t}^*$ .
  - 5:   Simulate  $S_{a,t+1} = S_{a,t}^M(S_{a,t}, P_{a,t}^*, W_{t+1}) \forall t \in \mathcal{D}_t = [t; t + \frac{(H+\Delta t)}{2}]$ , using Algorithm 1
  - 6:   Update forecasts in  $B_{a,t}$
  - 7:   Move time window  $\mathcal{D}_t^\pi \leftarrow \mathcal{D}_t^\pi + \frac{(H+\Delta t)}{2}$ ;
  - 8: **end for**
- 

the spot market in which the building participates. This is represented in the grid cost  $C_{\text{grid}}$  defined in Eq. 3. The grid power  $P_{\text{grid}}$  is included in the state vector  $S_t$ .

The system is composed of a 5kWp SPV, a 20kWh BESS with nickel manganese cobalt oxides (NMC) or Lithium iron phosphate (LFP) cells, two 12.5kW EV charging points, a 4kWe heat pump, a 2.7kWth solar thermal collector, a 200kWh TESS, a 6kWp electrical load, a 1kWp thermal demand, and 10kW LV grid connection. Power consumption profiles ( $P_{\text{load}}^c$ ) were constructed for a year using data from 2021 to 2023 from the TU Delft's Green Village smart meter data [38]. The output of the SPV is taken from [39, 40], the market prices  $\lambda$  are taken from the EPEX day-ahead auction, and  $\lambda_{\text{buy}} = 0.95\lambda_{\text{sell}}$  [41], and the heat demand  $P_{\text{load}}^{\text{th}}$  was modeled as [42].

The cells used are SANYO NCR18650 cells for NMC as in [15] and A123 cells for LFP. Their datasets were taken from PyBaMM [43] and LiBRA [35]. To construct the ECM for both cell types synthetic/simulated cells were built and simulated in PyBaMM using standard 1D full order model (FOM). The simulations followed the testing methodology from Plett, Chapter 2 Sections 2.9-11, [17]. Once the simulated profiles are ready the ECM parameters can be identified using subspace system identification as in [44]. The parameters can be found in Appendix A, Table A.5.

The OCP and simulations were modelled and run using Julia [45], JuMP [46], and InfiniteOpt [47]. The chosen solver was KNITRO from Artelys since it can handle MINLP formulations and NLP with complementarity constraints [48].

### 5.1. Case Study I: Day-ahead planning

To test and validate our EMA the planner was simulated for two standard months (summer and winter) using 2023 data from the previously mentioned sources.

To quantify the impact of each performance and aging model 5 day-ahead planners were built:

- (BNoDeg) Including a bucket model and no degradation.  $\tilde{S}_{a,t}^{M1}$ .
- (CEmpDeg) Including a first-order ECM and empirical aging for the *sa*.  $\tilde{S}_{a,t}^{M2}$ .
- (CPBDeg) Including first-order ECM with PBROM aging for the *sa*.  $\tilde{S}_{a,t}^{M3}$ .

– (-w11), where weights are  $w_{\text{grid}} = w_{\text{loss}} = 1$ .

The simulation workflow is presented in Algorithm 2 and depicted in Fig. 2. First, the hyperparameters are initialized. This includes the time window to be optimized  $\mathcal{D}_t^\pi = [t; t + H]$ , weights  $w$ , number of days  $n_d$ , user preferences, the initial state  $S_{a,0}$ , etc. In our case for day-ahead planning, the time window is  $H = 48\text{hr} - \Delta t$  and  $n_d = 29$ . At timestep  $t$  the OCP in Eq. 9, is solved obtaining the actions sequence  $\mathcal{P}_{a,[t,t+(H+\Delta t)/2]}^*$ . Together with the exogenous information sequence  $\mathcal{W}_{[t+1,t+(H+\Delta t)/2]}$  the actions are passed to the simulator  $S_{a,t}^M$  to get the feedback state sequence  $S_{a,[t,t+(H+\Delta t)/2]}$ . This feedback loop is repeated  $n_d$  times.

As a representative example Fig. 6 presents the results for the *CPBDeg-w11* planner for a monthly period. It has the resulting power balances (electrical and thermal) and the use of the HESS. The electric ESS have daily cycles to minimize operating costs (energy arbitrage). This is particularly important for the EV since its mobility demand already establishes a daily periodicity. Thus, due to the EV's battery pack size and its natural periodicity, it becomes the main electric storage of the system. This frees up the BESS for energy arbitrage, which tries to capture prices variations when possible within the power balance. Thus price volatility incentivizes cycling. However, due to the SEI model, batteries are also pushed downwards to the minimum aging state at  $\underline{SoC}_{sa,t}$ . Thus the dispatch contemplates a trade-off between the 2 parts of the objective  $C_{\text{grid}}$  and  $Q_{\text{loss}}$ . During the summer, price volatility is high with several hours with  $\lambda \leq 0$ , the EMS buys this energy to reduce costs. In winter, prices are less volatile and the load is higher leading to less opportunities for arbitrage and overall higher costs.

On the thermal side, the natural periodicity of the carrier is longer. Thus during the first week the initial  $SoC_{\text{TESS},0}$  influences costs greatly. After the first week the EMS has already steered the buffer to its desired setpoint. This means a high  $SoC_{\text{TESS},t}$  during summer (high heat generation, low load) and a low setpoint during winter (low heat generation, high load). The high setpoint during summer entails 2 risks: overcharging the TESS (i.e. activating soft-constraint) and not capturing negative prices/highly volatile prices due to past short-sight (TESS starting a day with a high  $SoC$ ).

The performance of the ESS under the different planners is summarized in Figs. 7- 9. The first two present the 2D histogram between  $SoC$  and  $P$  of the electrical storages whereas the third presents the timeseries of the TESS. In the histograms the left-hand side is for charge ( $P \leq 0$ ) and the right-hand side is for discharge ( $P \geq 0$ ). For the BESS, Fig. 7, the *BNoDeg* and *CEmpDeg* cycle the battery pack more often, spreading towards the edges of  $P_{\text{BESS},t}$  and  $SoC$ . The *CPBDeg* planner cycles less frequently, concentrating the operation near  $P = 0$  and  $\underline{SoC}$  to reduce the ageing of the BESS. This is true for both summer (top) and winter (bottom).

For the EV 2D histograms, Fig.8, the driving power  $P_{\text{drive,EV}}$  is excluded and only the moments where the car is connected are analyzed ( $P_{\text{EV},t}, \gamma_{\text{EV},t}$ ). The user's mobility requirement leads to similar distributions for all the planners, with this denser distribution on the left half-plane for charging. Its shape can be explained by the fact that all planners try to delay the charging to extend the V2G as much as possible. V2G mode

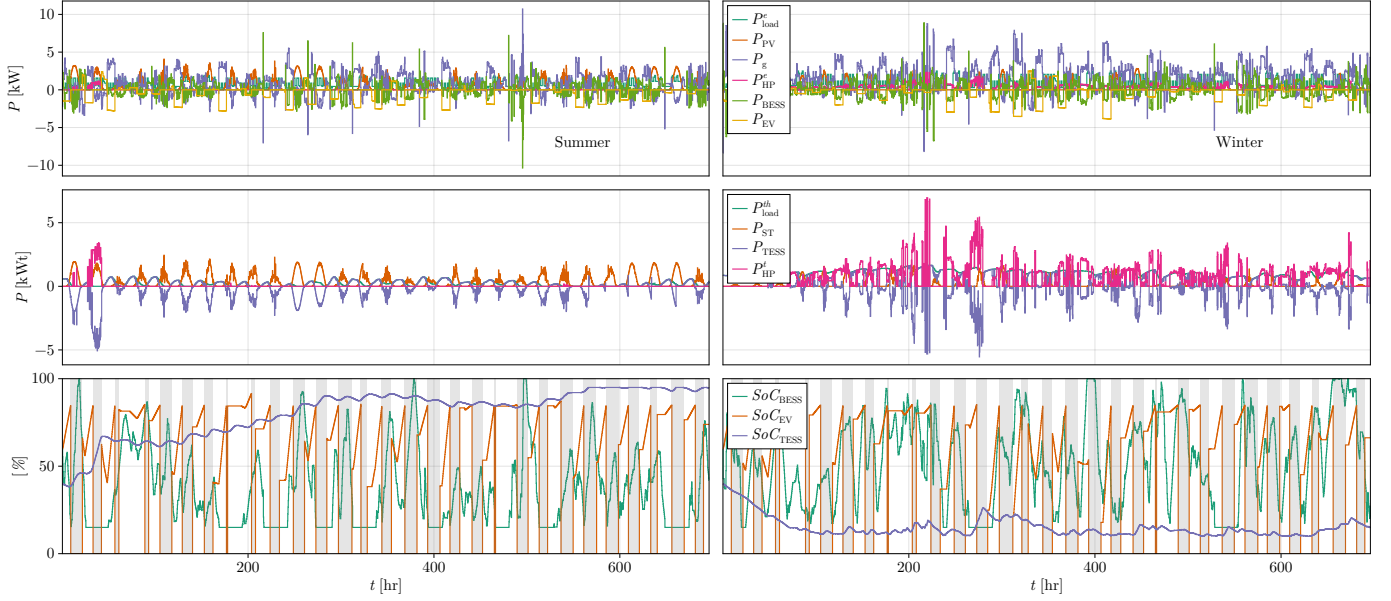


Figure 6: Monthly dispatch of MCES under CPBDeg-DA planner for summer (left) and winter (right).

is less frequent in the *BNoDeg/CEmpDeg* than in the *CPBDeg-w11*. This occurs in both standard seasons. In summary, the operation pattern of the EV is dominated by its mobility demand. Finally, for the TESS, Fig. 9 shows that in the summer the *CPBDeg-w11* has the smallest ST curtailment, because the chosen trajectory is the lowest of the three. *BNoDeg* and *CEmpDeg* chose almost the same trajectory for  $SoC_{TESS,t}$ .

The performance of each planner is summarized in Table 1. Starting with the grid cost  $C_{grid}$ , the best performer is the *CEmpDeg* in the summer and *BNoDeg* in the winter. The differences between first and second are less than 1 €. The worst performer is *CPBDeg-w11*. For the total capacity fade  $Q_{loss}$ , *CEmpDeg* has the highest degradation in the summer and *BNoDeg* has the highest in the winter. The proposed aging aware *CPBDeg* achieves the lowest degradation in both seasons maintaining a reasonable  $C_{grid}$ .

In general the planner that has the lowest  $C_{grid}$  is the one with the highest  $Q_{loss}$ , but this is not always *BNoDeg*. The *CEmpDeg* fails to minimize the total capacity fade because of its model bias ( $S_{a,t}^M \neq \tilde{S}_{a,t}^M$ ), in which it is rewarded to cycle at  $\bar{SoC}_{sa}$  and a calendar ageing independent of the  $SoC_{sa,t}$ . Additionally the linear *BNoDeg* planner fails to fulfill its predictions because of the high number of rejected actions during summer. This is because when the *BNoDeg* plans for high-power discharges its predicted  $\tilde{SoC}_{sa,t}$  deviates from the true  $SoC_{sa,t}$  of the simulator  $S_{a,t}^M$ , wrongly depleting the ESS early (lower bound  $\underline{SoC}_{sa,t}$ ). The linear *BNoDeg* is the planner with the highest percentage of rejects, roughly 45% of the total time in the summer.

However, when looking at the total storage usage, one must also analyze the number of cycles done by the *sa*. Figure 10 presents the full equivalent cycles  $FEC$  over time  $t$ , showing that the *CPBDeg* planners increase the EV usage  $FEC_{EV}$  at the expense of doing less cycles with the BESS. When analyzing the capacity fade  $Q_{loss}$  against the full eq. cycles  $FEC$ , Fig.

Planner	$C_g$ [€]		$Q_{loss}$ [mAh]	
	summer	winter	summer	winter
<b>BNoDeg</b>	16.01	77.33	206.9	249.2
<b>CEmpDeg</b>	15.22	77.45	216.4	236.7
<b>CPBDeg_W11</b>	20.28	78.25	206.6	234.3

Table 1: Planner comparison cost summary.

10, it is clear that the relative degradation per cycle ( $\frac{\partial Q_{loss}}{\partial FEC}$ ) of the *CPBDeg* is smaller in the winter than the used benchmarks. In summer, the *BNoDeg* has the lowest degradation per cycle due to its high number of rejects. The use of the EVs is the same for all planners, because the trajectory is mostly driven by user mobility. Finally, in both seasons *CEmpDeg* presents the highest  $\frac{\partial Q_{loss}}{\partial FEC}$ . This appears to be as a risky strategy due to a lack of consistency across season and objectives (minimizing degradation or minimizing grid costs).

Finally, the computational time for the different strategies is presented in Fig. 11. Each sample is the total computational time it takes to solve Algorithm 2. Unexpectedly, *BNoDeg* has the lowest and most consistent  $t_{comp}$  distribution. However both *CEmpDeg* and *CPBDeg* planners have similar distributions, maintaining overall fast computational time, indicating that the modeling accuracy of *CPBDeg* is not prohibitively expensive.

## 5.2. Case Study II: Managing different cathodes

To demonstrate the PB models' flexibility and extended capabilities, the *CPBDeg* scheduler is tested using two similar battery packs of the same rated capacity  $Q$  but using different cells. One is formed with NMC cells and the other with LFP. Since LFP cells have a lower rated capacity of  $Q_n = 2.3$  Ah and a lower OCV, the battery packs have more  $N_{s/p}$  to have roughly the same pack-rated capacity as its NMC counterparts.

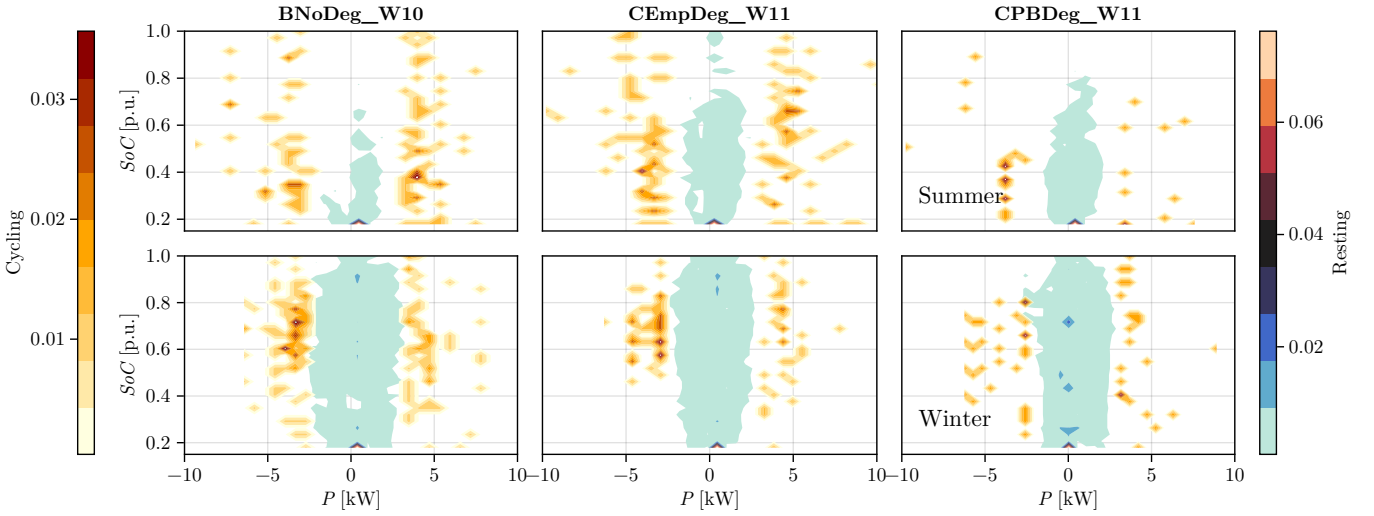


Figure 7: Normalized 2D histogram of  $SoC$  and  $P$  for the BESS under the different DA planners.

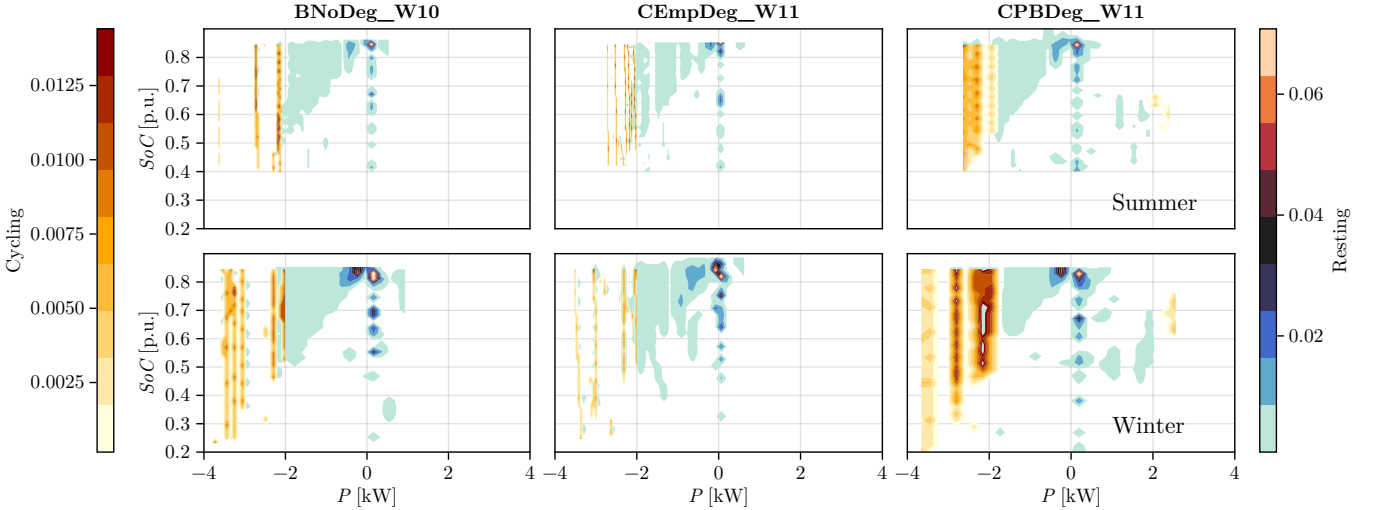


Figure 8: Normalized 2D histogram of  $SoC$  and  $P$  for the EV under the different DA planners.

The power limits  $\bar{P}_{sa,t}$ ,  $\underline{P}_{sa,t}$  are also maintained to make an even comparison.

The PB aging models are suitable for both because they have graphite anodes [15, 23]. Nevertheless, they have different electrolytes. This is addressed by changing the electrolyte parameters in the model. Thus we use the same model equations but with different parameter values. This is a great advantage compared to the empirical fits presented in the literature. In the latter, the derived models are prone to overfitting to training conditions, delivering complex non-linear equations that can only be applied to specific chemistries, battery pack designs, and operating conditions. For our *CPBDeg* the physical parameters of the LFP cell used are taken from [24] and can be found in Appendix A, Tables A.4 and A.5.

The simulation results are presented in Figs. 12 - 13a. Starting with the EV, Fig. 12a, the operation is similar except for

a few days in summer and winter in which the LFP decides to have deeper discharges than its NMC counterpart. Moving forward to the BESS, Fig. 12b, in summer the LFP scheduler is too ambitious generating early storage depletion roughly 40% of the time, 10% more than the NMC cells. During the winter total rejections are reduced to 25% and 10% for LFP and NMC respectively.

Continuing with the ageing analysis Fig. 13a presents the  $FEC$  and  $Q_{loss}$  results. When looking at the EV, the  $FEC_{EV}$  increases with the LFP cells. The opposite happens to the BESS, which reduces its cycles in the LFP pack. In combination with its lower calendar ageing, represented in the parameter set, the LFP packs achieve lower degradation per eq. cycle  $\frac{\partial Q_{loss}}{\partial FEC}$  than their NMC counterpart. As such, the *CPBDeg-LFP* reduces BESS total throughput ( $FEC$ ) and capacity fade  $Q_{loss}$  while increasing EV throughput and reducing its degradation.

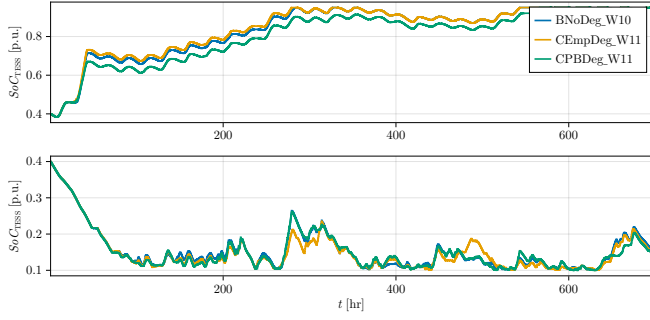


Figure 9: Monthly simulation  $SoC_{TESS}$  for summer (top) and winter (bottom).

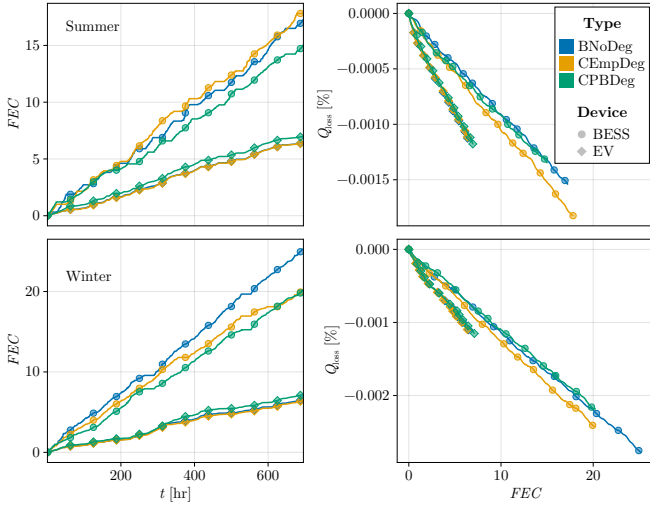


Figure 10: Full equivalent cycles  $FEC$  over time (left) and relative capacity fade  $Q_{loss}$  over  $FEC$  (right).

Table 2 presents the summary of performance for both cell types. Overall the  $CPBDeg$ -LFP achieve lower total costs and ageing despite their high number of rejected actions. During winter  $C_{grid}$  stays the same with 37% less degradation. However, in the summer, just by changing the cell type from NMC to LFP  $C_{grid}$  is reduced by 25%, similar to  $BNoDeg$  in Section 5.1 1, and roughly 25% less capacity fade. This shows that  $CPBDeg$  rightly exploits its physical information of the system to achieve better performance.

### 5.3. Case Study III: Managing aged and fresh batteries

To demonstrate the flexibility and extended capabilities of the  $CPBDeg$  planner the scheduler is tested using two battery packs: the first is the fresh battery pack of NMC cells of Section 5.1 and the second is the same pack but with cells aged at

Cell cathode	$C_g$ [€]		$Q_{loss}$ [mAh]	
	summer	winter	summer	winter
LFP	15.25	78.36	152.1	147.1
NMC	20.28	78.25	206.6	234.3

Table 2: Cathode comparison cost summary.

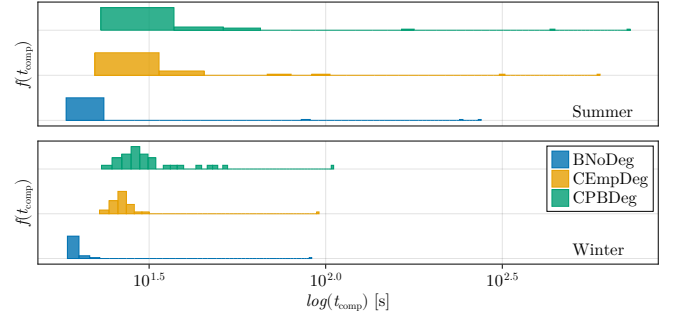


Figure 11: Distributions of computational time  $t_{comp}$ .

$SoH = 90\%$ . Only one benchmark is used: a  $BNoDeg$  with no  $SoH$  update. Thus, the  $BNoDeg$  EMS sees a perfectly healthy cell with rated capacity when in reality the battery pack is aged 10%. The update is based on a 5% increase in series resistance  $R_{sa,0}$  and 10% decrease of the available Li content  $z_{100\%,sa}$ .

Figure 13b presents the degradation patterns for the 2 planners and different  $SoH$ . In the aged battery, the share of calendar ageing (against the total) is much smaller and thus the percentual  $Q_{loss}$  is almost 35% smaller than in the new battery packs. In both seasons, the EVs patterns are similar for both  $BNoDeg$  and  $CPBDeg$ . The change in EV trajectories between aged and fresh cells shows slight increase  $FEC$ , due to smaller rated capacity, and a decrease in relative ageing, due to reduced calendar ageing. The impact on the BESS is more pronounced. In winter,  $CPBDeg$  has smaller  $\frac{\partial Q_{loss}}{\partial FEC}$  (upper-right hand side of the graph) for both aged and new cells with  $BNoDeg$  doing more eq. cycles. In the winter  $CPBDeg$  still has a smaller  $\frac{\partial Q_{loss}}{\partial FEC}$  in the new cell but not in the used cell, where this is achieved by the benchmark controller.

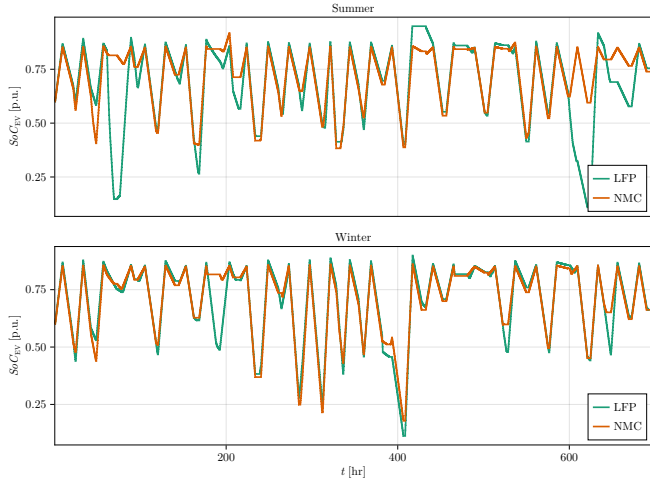
However when adding the costs to the analysis, summarized in Table 3, it is noticed that:

- $CPBDeg$  achieves lower capacity fade  $Q_{loss}$  than  $BNoDeg$  across all seasons and  $SoH$ .
- $CPBDeg$  improves its total grid cost  $C_{grid}$  as the cells degrade, in particular during summer.
- $BNoDeg$  worsens its performance as the cells degrade. With higher  $C_{grid}$ ,  $Q_{loss}$  and model bias.

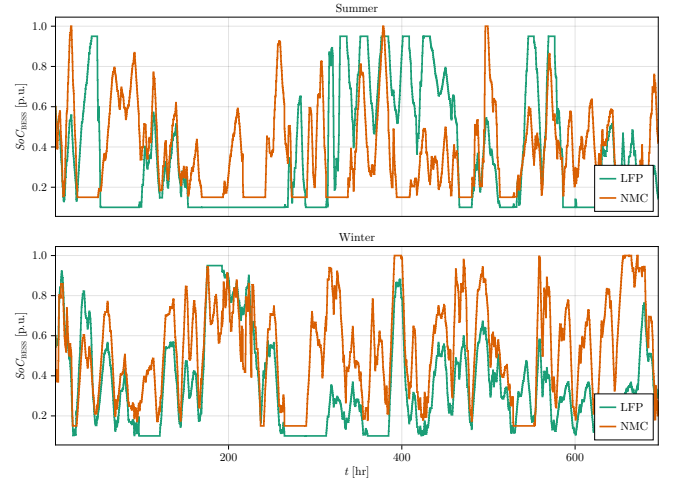
In summary, the performance of the proposed  $CPBDeg$  planner comparatively improves when using used cells, with respect to its linear  $BNoDeg$  benchmark.

## 6. Conclusions & Discussion

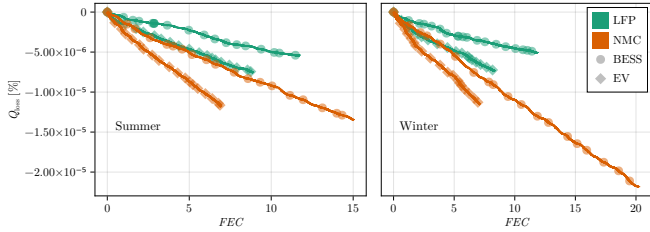
In summary, this paper presents an optimization-based day-ahead planner for residential multi-carrier energy systems that uses PBROM models to integrate battery ageing. The proposed  $CPBDeg$  planner can handle different cathode chemistries as well as batteries in different ageing states. The planner does this with lower degradation than the its benchmarks. This comes the expense of slightly higher computational times and grid cost.



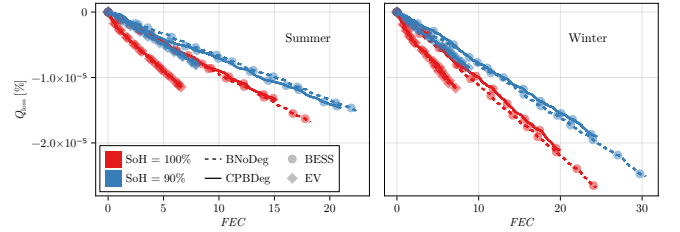
(a)



(b)

Figure 12: Cathode comparison simulation a)  $SoC_{nEV}$  and b)  $SoC_{BESS}$ .

(a) Case Study 2 - LFP and NMC cells.



(b) Case Study 3 - new and aged cells.

Figure 13: Degradation analysis  $Q_{loss,t}$  vs  $FEC$ 

Planner	$C_g$ [€]		$Q_{loss}$ [mAh]	
	summer	winter	summer	winter
SoH 100 %				
CPBDeg	24.7	79.0	202.0	232.8
BNoDeg	14.9	76.9	212.0	243.6
SoH 90 %				
CPBDeg	16.3	78.7	130.0	149.0
BNoDeg	15.2	77.6	132.3	158.3

Table 3: Cost and degradation summary.

In the first case study it is shown how advanced PBROM can be used to reduce battery ageing while maintaining a reasonable grid cost, in accordance to the literature for standalone utility-scale applications [21, 28, 29, 49, 50]. This is because the planner can control the degradation per full equivalent cycle better than the benchmarks.

In the second case study, the proposed planner is equipped with battery packs of different cathode chemistries and its performance is compared. This is out of the scope of most empirical degradation models. The LFP battery pack has a lower total  $Q_{loss}$  as per established knowledge and can achieve lower grid costs  $C_{grid}$  than its NMC counterpart. Even more so, when considering that the relative cost  $c_{loss}$  used for both packs was

the same, when in reality LFP packs have a lower cost than NMC packs. Thus the 5.2 is a conservative approximation and LFP packs have the potential to enable even lower operation costs. This is achieved just by changing some simple parameter models taken from the literature. This is an important feature because it allows the EMS to fully exploit any battery pack at hand. During the last case study it was shown how the proposed EMA handles aged and new batteries seamlessly, even improving performance. Its linear counterpart however is unaware of the degradation, increasing the number of rejected actions. Summing up reducing the grid costs can be achieved by using LFP battery packs or modifying objective weights, the latter at the expense of higher degradation.

It is worth noting again that in this work only one optimization is done per day for all models (benchmarks and novel). If re-optimizations occur frequently as in MPC, model bias can be mitigated. Future works will seek to implement the proposed models in an economic MPC approach. Moreover, for physical setups the proposed physics-based approach requires a non-linear observer to identify internal states and a system identification algorithm to parametrize the models. Adaptive control techniques/ online learning techniques are crucial for scaling implementation. For the case of the BESS initial tests and model identification can be done offline before start-up, and even offline during operation if historic data is continuously

stored. However, for EVs models, parametrization deems a challenge since a previously unknown car may appear or due to unknown driving conditions and profiles. Thus, the development of effective and accurate observers to identify and parametrize PBROM online automatically is crucial. This allows the EMS predictions to be closer to reality, minimizing setpoint rejection by the BMS [17, 18, 37].

Another limitation of the proposed EMA is the modelling of the thermal carrier. In this paper, all thermal devices are assumed linear, and the horizon window  $H$  is only 48hs. Thus seasonal and monthly variations can not be handled properly [51] as in other studies, like long-term hydrothermal dispatch problems [52]. Future works will address this shortcoming and improve the thermal models for seasonal planning [20, 42].

## Appendix A. Appendix: A

Graphite anode open-circuit voltage:

$$\begin{aligned}
 OCV_{n,sa,t}(z_{sa,t}) = & 0.6379 + 0.5416 \cdot e^{-305.5309 \cdot z_{sa,t}} \\
 & + 0.044 \cdot \tanh\left(-\frac{z_{sa,t} - 0.1958}{0.108}\right) \\
 & - 0.1978 \cdot \tanh\left(\frac{z_{sa,t} - 1.0571}{0.0854}\right) \\
 & - 0.6875 \cdot \tanh\left(\frac{z_{sa,t} + 0.0117}{0.0529}\right) \\
 & - 0.0175 \cdot \tanh\left(\frac{z_{sa,t} - 0.5692}{0.0875}\right)
 \end{aligned} \quad (A.1)$$

Table A.4 presents the model parameters for the PBROMs.

For the first-order ECMs the model parameters are presented in Table A.5.

## References

- [1] IEA, Net Zero by 2050: A Roadmap for the Global Energy Sector, International Energy Agency (2021) 224.
- [2] M. Geidl, G. Andersson, Optimal Power Flow of Multiple Energy Carriers, *IEEE Transactions on Power Systems* 22 (1) (2007) 145–155. doi:10.1109/TPWRS.2006.888988. URL <https://ieeexplore.ieee.org/document/4077107/>
- [3] G. Andersson, E. Zurich, M. Geidl, Optimal power dispatch and conversion in systems with multiple energy carriers PlanGridEV View project BPES-Optimal sizing and control of balancing power in the future EU power system considering transmission constraints View project OPTIMAL POWER DISPATCH, Proceedings 15th Power Systems Computation Conference (PSCC). (2005). URL <https://www.researchgate.net/publication/228776936>
- [4] W. Vermeer, G. R. C. Mouli, P. Bauer, Real-Time Building Smart Charging System Based on PV Forecast and Li-Ion Battery Degradation, *Energies* 2020, Vol. 13, Page 3415 13 (13) (2020) 3415. doi:10.3390/EN13133415. URL <https://www.mdpi.com/1996-1073/13/13/3415/htm><https://www.mdpi.com/1996-1073/13/13/3415>
- [5] W. Vermeer, G. R. Chandra Mouli, P. Bauer, A Comprehensive Review on the Characteristics and Modeling of Lithium-Ion Battery Aging, *IEEE Transactions on Transportation Electrification* 8 (2) (2022) 2205–2232. doi:10.1109/TTE.2021.3138357. URL <https://ieeexplore.ieee.org/document/9662298/>
- [6] G. Ceusters, R. C. Rodríguez, A. B. García, R. Franke, G. Deconinck, L. Helsen, A. Nowé, M. Messagie, L. R. Camargo, Model-predictive control and reinforcement learning in multi-energy system case studies, *Applied Energy* 303 (2021) 117634. doi:10.1016/j.apenergy.2021.117634. URL <https://linkinghub.elsevier.com/retrieve/pii/S0306261921010011>
- [7] G. Ceusters, L. R. Camargo, R. Franke, A. Nowé, M. Messagie, Safe reinforcement learning for multi-energy management systems with known constraint functions, *Energy and AI* 12 (2023) 100227. doi:10.1016/j.egyai.2022.100227. URL <https://doi.org/10.1016/j.egyai.2022.100227><https://linkinghub.elsevier.com/retrieve/pii/S2666546822000738>
- [8] D. Van Der Meer, G. R. C. Mouli, G. M. E. Mouli, L. R. Elizondo, P. Bauer, Energy Management System with PV Power Forecast to Optimally Charge EVs at the Workplace, *IEEE Transactions on Industrial Informatics* 14 (1) (2018) 311–320. doi:10.1109/TII.2016.2634624.
- [9] Y. Ye, D. Qiu, X. Wu, G. Strbac, J. Ward, Model-Free Real-Time Autonomous Control for a Residential Multi-Energy System Using Deep Reinforcement Learning, *IEEE Transactions on Smart Grid* 11 (4) (2020) 3068–3082. doi:10.1109/TSG.2020.2976771. URL <https://ieeexplore.ieee.org/document/9016168/>
- [10] W. Vermeer, G. R. C. Mouli, P. Bauer, Optimal Sizing and Control of a PV-EV-BES Charging System Including Primary Frequency Control and Component Degradation, *IEEE Open Journal of the Industrial Electronics Society* 3 (2022) 236–251. doi:10.1109/OJIES.2022.3161091. URL <https://ieeexplore.ieee.org/document/9740621/>
- [11] W. Vermeer, G. R. Chandra Mouli, P. Bauer, A Multi-Objective Design Approach for PV-Battery Assisted Fast Charging Stations Based on Real Data, 2022 IEEE Transportation Electrification Conference and Expo, ITEC 2022 (2022) 114–118doi:10.1109/ITEC53557.2022.9814016.
- [12] A. Esmael Nezhad, A. Rahimnejad, P. H. J. Nardelli, S. A. Gadsden, S. Sahoo, F. Ghanavati, A Shrinking Horizon Model Predictive Controller for Daily Scheduling of Home Energy Management Systems, *IEEE Access* 10 (2022) 29716–29730. doi:10.1109/ACCESS.2022.3158346. URL <https://ieeexplore.ieee.org/document/9732346/>
- [13] P. Alexeenko, E. Bitar, Achieving reliable coordination of residential plug-in electric vehicle charging: A pilot study, *Transportation Research Part D: Transport and Environment* 118 (2023) 103658. doi:10.1016/j.trd.2023.103658. URL <https://linkinghub.elsevier.com/retrieve/pii/S136192092300055X>
- [14] M. A. Xavier, A. K. de Souza, K. Karami, G. L. Plett, M. S. Trimboli, A Computational Framework for Lithium Ion Cell-Level Model Predictive Control Using a Physics-Based Reduced-Order Model, *IEEE Control Systems Letters* 5 (4) (2021) 1387–1392. doi:10.1109/LCSYS.2020.3038131. URL <https://www.ieee.org/publications/rights/index.html><https://ieeexplore.ieee.org/document/9259035/>
- [15] X. Jin, Aging-Aware optimal charging strategy for lithium-ion batteries: Considering aging status and electro-thermal-aging dynamics, *Electrochimica Acta* 407 (2022) 139651. doi:10.1016/j.electacta.2021.139651. URL <https://linkinghub.elsevier.com/retrieve/pii/S0013468621019356>
- [16] Y. Li, Y. Yang, J. Tang, B. Xiong, X. Deng, D. Tang, Design of Degradation-Conscious Optimal Dispatch Strategy for Home Energy Management System With Rooftop PV and Lithium-Ion Batteries, in: 2019 4th International Conference on Intelligent Green Building and Smart Grid (IGBSG), IEEE, 2019, pp. 741–746. doi:10.1109/IGBSG.2019.8886194. URL <https://ieeexplore.ieee.org/document/8886194/>
- [17] G. L. Plett, Battery Management Systems Volume I Battery Modeling, Artech House Power Engineering and Power Electronics, 2015. URL <https://us.artechhouse.com/Battery-Management-Systems-Volume-1-Battery-Modeling-P1752.aspx>
- [18] G. L. Plett, BATTERY MANAGEMENT SYSTEMS Volume II: Equivalent-Circuit Methods, first edit Edition, Artech House Power



Parameter	Description	Units	NMC (SANYO cell)	LFP (A123 cell)
$n_{SEI}$	Number of $e^-$ transferred in SEI side reaction	-		2.0
$\lambda$	Constant $\lambda = \frac{c_s \sqrt{D_s}}{c_p \sqrt{D_p}}$	-		$5.51 \times 10^{-5}$
$OCV_s$	OCV of the side reaction	V		0.4
$\varepsilon_{AM}$	Active material volume fraction	-		0.552
$R_s$	Particle radius	m	$7.5 \times 10^{-6}$	$5 \times 10^{-6}$
$a_s$	Specific surface area of the anode	$m^{-1}$		$\frac{3 \cdot \varepsilon_{AM}}{R_s}$
$A_n$	Active surface area of the anode	$m^2$	0.105	0.18
$L_n$	Thickness of anode	m	$50 \times 10^{-6}$	$34 \times 10^{-6}$
$i_0$	Exchange current of the intercalation current	$A/m^2$		1.5
$k_{SEI}$	Kinetic rate	$1/\sqrt{s}$		66.85
$E_{SEI}$	Activation energy	J/mol		39146.0
$\delta_{SEI,0}$	Initial value of the SEI layer thickness	m		$2.0 \times 10^{-9}$
$M_{SEI}$	Molecular weight of the SEI layer	kg/mol		0.162
$\rho_{SEI}$	Density of the SEI layer	$kg/m^3$		1690.0
$z_{100\%}$	Full electrode stoichiometry	-	0.9	0.81
$z_{0\%}$	Empty electrode stoichiometry	-	0	0.0176
$k_{AM}$	Kinetic rate	1/Ah		0.0137
$E_{AM}$	Activation energy	J/mol		39500.0
$\beta$	Tuning parameter	-		1.7
$t_0^+$	Transport/transference number	-	0.363	0.36
$E_\kappa$	Activation energy for $\kappa$	J/mol		34700.0
$E_{D_e}$	Activation energy for $D_e$	J/mol		34700.0
$\kappa_{ref}$	Reference ionic conductivity for $\kappa$ at reference temperature	S/m		0.174
$D_{e,ref}$	Reference value for $D_e$ at reference temperature	$m^2/s$		$7.5 \times 10^{-11}$
$brug$	Bruggeman coefficient	-		3/2
$c_{e,avg}$	Average volume concentration of Li in the electrolyte	$mol/m^3$	1000	1200
$c_{e,max}$	Maximum volume concentration of Li in the electrolyte	$mol/m^3$	1000	1200
$\sigma_n$	Electronic conductivity	S/m	100	215
$\varepsilon_s$	Volume fraction of solid electrolyte	-	0.59	0.58

Table A.4: Parameter values, descriptions, and units for PBROMs.

Parameter	Unit	NMC (SANYO cell)	LFP (A123 cell)
$\eta_c$	%	99.5	99.9
$Q_0$	Ah/cell	5.29	2.29
$R_0$	$m\Omega$	28.11	27.01
$\tau_1 = R_1 C_1$	s	2.35	2.13
$R_1$	$m\Omega$	33.57	26.98

Table A.5: Parameter values, descriptions, and units for ECMs.

- Engineering and Power Electronics, 2016.  
URL <https://us.artechhouse.com/Battery-Management-Systems-Volume-II-Equivalent-Circuit-Methods-P2192.aspx>
- [19] Z. Chen, L. Wu, Y. Fu, Z. Chen, L. Wu, Real-Time Price-Based Demand Response Management for Residential Appliances via Stochastic Optimization and Robust Optimization, IEEE Transactions on Smart Grid 3 (2012). doi:10.1109/TSG.2012.2212729.
- [20] M. J. Risbeck, Mixed-Integer Model Predictive Control with Applications to Building Energy Systems (2018).
- [21] J. M. Reniers, G. Mulder, D. A. Howey, Review and Performance Comparison of Mechanical-Chemical Degradation Models for Lithium-Ion Batteries, Journal of The Electrochemical Society 166 (14) (2019) A3189–A3200. doi:10.1149/2.0281914jes.  
URL <https://iopscience.iop.org/article/10.1149/2.0281914jes>
- [22] S. E. J. O’Kane, W. Ai, G. Madabattula, D. Alonso-Alvarez, R. Timms, V. Sulzer, J. S. Edge, B. Wu, G. J. Offer, M. Marinescu, Lithium-ion battery degradation: how to model it, Physical Chemistry Chemical Physics 24 (13) (2022) 7909–7922. doi:10.1039/D2CP00417H.  
URL <http://xlink.rsc.org/?DOI=D2CP00417H>
- [23] X. Jin, A. Vora, V. Hoshing, T. Saha, G. Shaver, R. E. García, O. Wasynczuk, S. Varigonda, Physically-based reduced-order capacity loss model for graphite anodes in Li-ion battery cells, Journal of Power Sources 342 (2017) 750–761. doi:10.1016/j.jpowsour.2016.12.099.  
URL <https://linkinghub.elsevier.com/retrieve/pii/S037877531631802X>
- [24] E. Prada, D. Di Domenico, Y. Creff, J. Bernard, V. Sauvant-Moynot, F. Huet, A Simplified Electrochemical and Thermal Aging Model of LiFePO<sub>4</sub>-Graphite Li-ion Batteries: Power and Capacity Fade Simulations, Journal of The Electrochemical Society 160 (4) (2013) A616–A628. doi:10.1149/2.053304JES/XML.  
URL <https://iopscience.iop.org/article/10.1149/2.053304jeshttps://iopscience.iop.org/article/10.1149/2.053304jes/meta>
- [25] J. Wang, J. Purewal, P. Liu, J. Hicks-Garner, S. Soukiazian, E. Sherman, A. Sorenson, L. Vu, H. Tataria, M. W. Verbrugge, Degradation of lithium ion batteries employing graphite negatives and nickel–cobalt–manganese oxide + spinel manganese oxide positives: Part 1, aging mechanisms and life estimation, Journal of Power Sources 269 (2014) 937–948. doi:10.1016/j.jpowsour.2014.07.030.  
URL <https://linkinghub.elsevier.com/retrieve/pii/S0378775314000000>



- S037877531401074X
- [26] D. Mariano-Hernández, L. Hernández-Callejo, A. Zorita-Lamadrid, O. Duque-Pérez, F. Santos García, A review of strategies for building energy management system: Model predictive control, demand side management, optimization, and fault detect & diagnosis, *Journal of Building Engineering* 33 (2021) 101692. doi:10.1016/J.JOBE.2020.101692.
- [27] J. Purewal, J. Wang, J. Graetz, S. Soukiazian, H. Tataria, M. W. Verbrugge, Degradation of lithium ion batteries employing graphite negatives and nickel-cobalt-manganese oxide + spinel manganese oxide positives: Part 2, chemical-mechanical degradation model, *Journal of Power Sources* 272 (2014) 1154–1161. doi:10.1016/J.JPOWSOUR.2014.07.028.
- [28] J. M. Reniers, D. A. Howey, Digital twin of a MWh-scale grid battery system for efficiency and degradation analysis, *Applied Energy* 336 (2023) 120774. doi:10.1016/J.APENERGY.2023.120774.  
URL <https://linkinghub.elsevier.com/retrieve/pii/S0306261923001381>
- [29] J. M. Reniers, G. Mulder, D. A. Howey, Unlocking extra value from grid batteries using advanced models, *Journal of Power Sources* 487 (December 2020) (2021) 229355. doi:10.1016/j.jpowsour.2020.229355.  
URL <https://doi.org/10.1016/j.jpowsour.2020.229355>  
<https://linkinghub.elsevier.com/retrieve/pii/S0378775320316438>
- [30] W. B. Powell, A unified framework for stochastic optimization, *European Journal of Operational Research* 275 (3) (2019) 795–821. doi:10.1016/J.EJOR.2018.07.014.
- [31] W. B. Powell, *Sequential Decision Analytics and Modeling Modeling with Python*, Now Foundations and Trends, 2022.
- [32] W. Powell, *Reinforcement Learning and Stochastic Optimization: A Unified Framework for Sequential Decisions*, Vol. 22, Wiley, 2022. doi:10.1080/14697688.2022.2135456.  
URL <https://www.tandfonline.com/doi/full/10.1080/14697688.2022.2135456>
- [33] L. Grüne, J. Pannek, *Nonlinear Model Predictive Control Theory and Algorithms*, 2017. doi:10.1007/978-3-319-46024-6.  
URL <http://www.springer.com/series/61>
- [34] Home - Elaad NL (2024).  
URL <https://platform.elaad.io/>
- [35] B. Planden, K. Lukow, P. Henshall, G. Collier, D. Morrey, A computationally informed realisation algorithm for lithium-ion batteries implemented with LiIBRA.jl, *Journal of Energy Storage* 55 (2022) 105637. doi:10.1016/j.est.2022.105637.  
URL <https://linkinghub.elsevier.com/retrieve/pii/S2352152X22016255>
- [36] A. Rodríguez, G. L. Plett, M. S. Trimboli, Comparing four model-order reduction techniques, applied to lithium-ion battery-cell internal electrochemical transfer functions, *eTransportation* 1 (2019) 100009. doi:10.1016/j.etrans.2019.100009.  
URL <https://linkinghub.elsevier.com/retrieve/pii/S2590116819300098>
- [37] G. Fan, D. Lu, M. S. Trimboli, G. L. Plett, C. Zhu, X. Zhang, Non-destructive diagnostics and quantification of battery aging under different degradation paths, *Journal of Power Sources* 557 (2023) 232555. doi:10.1016/J.JPOWSOUR.2022.232555.
- [38] The Green Village, fieldlab voor duurzame innovatie.  
URL <https://www.thegreenvillage.org/>
- [39] A. Smets, K. Jäger, O. Isabella, R. van Swaaij, M. Zeman, *Solar Energy: The physics and engineering of photovoltaic conversion, technologies and systems*, UIT Cambridge Ltd, 2016.  
URL <https://ebookcentral-proquest-com.tudelft.idm.oclc.org/lib/delft/detail.action?docID=4781743>
- [40] I. Diab, A. Saffirio, G. R. Chandra-Mouli, P. Bauer, A simple method for sizing and estimating the performance of PV systems in trolleybus grids, *Journal of Cleaner Production* 384 (2023) 135623. doi:10.1016/J.JCLEPRO.2022.135623.
- [41] EPEX Spot (2023).  
URL <https://www.epexspot.com/en>
- [42] J. Alpízar-Castillo, L. M. Ramírez-Elizondo, P. Bauer, Modelling and evaluating different multi-carrier energy system configurations for a Dutch house, *Applied Energy* 364 (2024) 123197. doi:10.1016/j.apenergy.2024.123197.  
URL <https://linkinghub.elsevier.com/retrieve/pii/S0306261924005804>
- [43] V. Sulzer, S. G. Marquis, R. Timms, M. Robinson, S. J. Chapman, Python battery mathematical modelling (PyBaMM), *Journal of Open Research Software* 9 (1) (2021) 1–8. doi:10.5334/JORS.309.  
URL <https://doi.org/10.5334/>
- [44] G. L. Plett, Extended Kalman filtering for battery management systems of LiPB-based HEV battery packs: Part 2. Modeling and identification, *Journal of Power Sources* 134 (2) (2004) 262–276. doi:10.1016/J.JPOWSOUR.2004.02.032.
- [45] J. Bezanson, A. Edelman, S. Karpinski, V. B. Shah, Julia: A Fresh Approach to Numerical Computing, *SIAM Review* 59 (1) (2017) 65–98. doi:10.1137/141000671.
- [46] M. Lubin, O. Dowson, J. D. Garcia, J. Huchette, B. Legat, J. P. Vielma, JuMP 1.0: Recent improvements to a modeling language for mathematical optimization (5 2022).  
URL <http://arxiv.org/abs/2206.03866>
- [47] J. L. Pulsipher, W. Zhang, T. J. Hongisto, V. M. Zavala, A unifying modeling abstraction for infinite-dimensional optimization, *Computers & Chemical Engineering* 156 (2022) 107567. doi:10.1016/j.compchemeng.2021.107567.
- [48] R. H. Byrd, J. Nocedal, R. A. Waltz, Knitro: An Integrated Package for Nonlinear Optimization, Springer, Boston, MA, 2006, pp. 35–59. doi:10.1007/0-387-30065-1\_{\_}4.  
URL [http://link.springer.com/10.1007/0-387-30065-1\\_4](http://link.springer.com/10.1007/0-387-30065-1_4)
- [49] J. M. Reniers, G. Mulder, S. Ober-Blöbaum, D. A. Howey, Improving optimal control of grid-connected lithium-ion batteries through more accurate battery and degradation modelling, *Journal of Power Sources* 379 (September 2017) (2018) 91–102. doi:10.1016/j.jpowsour.2018.01.004.  
URL <https://doi.org/10.1016/j.jpowsour.2018.01.004>  
<https://linkinghub.elsevier.com/retrieve/pii/S0378775318300041>
- [50] J. Reniers, Degradation-aware optimal control of grid-connected lithium-ion batteries, Ph.D. thesis, University of Oxford (2020).
- [51] E. Prat, R. M. Lusby, J. M. Morales, S. Pineda, P. Pinson, How long is long enough? Finite-horizon approximation of energy storage scheduling problems (11 2024).  
URL <http://arxiv.org/abs/2411.17463>
- [52] A. W. Rosemberg, A. Street, J. D. Garcia, D. M. Valladao, T. Silva, O. Dowson, Assessing the Cost of Network Simplifications in Long-Term Hydrothermal Dispatch Planning Models, *IEEE Transactions on Sustainable Energy* 13 (1) (2022) 196–206. doi:10.1109/TSTE.2021.3106810.  
URL <https://ieeexplore.ieee.org/document/9521833/>